

Article

Energy Storage System Event-Driven Frequency Control Using Neural Networks to Comply with Frequency Grid Code

Soseul Jeong ¹, Junghun Lee ¹, Minhan Yoon ² and Gilsoo Jang ^{1,*} 

¹ School of Electrical Engineering, Korea University, Seoul 02841, Korea; jss928@korea.ac.kr (S.J.); ejh1015@korea.ac.kr (J.L.)

² Department of Electrical Engineering, Kwangwoon University, Seoul 01897, Korea; minhan.yoon@gmail.com

* Correspondence: gjang@korea.ac.kr; Tel.: +82-02-3290-3264; Fax: +82-2-3290-3692

Received: 12 March 2020; Accepted: 30 March 2020; Published: 2 April 2020



Abstract: As the penetration of renewable energy sources (RESs) increases, the rate of conventional generators and the power system inertia are reduced accordingly, resulting in frequency-stability concerns. As one of the solutions, the battery-type energy storage system (ESS), which can rapidly charge and discharge energy, is utilized for frequency regulation. Typically, it is based on response-driven frequency control (RDFC), which adjusts its output according to the measured frequency. In contrast, event-driven frequency control (EDFC) involves a determined frequency support scheme corresponding to a particular event. EDFC has the advantage that control action is promptly performed compared to RDFC. This study proposes an ESS EDFC strategy that involves estimating the required operating point of the ESS according to a specific disturbance through neural-network training. When a disturbance occurs, the neural networks can estimate the proper magnitude and duration of the ESS output to comply with the frequency grid code. A simulation to validate the proposed control method was performed for an IEEE 39 bus system. The simulation results indicate that a neural-network estimation offers sufficient accuracy for practical use, and frequency response can be adjusted as intended by the system operator.

Keywords: ESS; frequency control; neural network; event-driven

1. Introduction

Recently, the power systems of the world have been changing significantly, as the penetration of renewable energy sources (RESs) has accelerated. Among the countries across the world, China has made the largest investment in RESs, and it plans to generate at least 35% of its electricity with RESs by 2030 [1]. Additionally, the European Union has increased its target for RESs from 27% to 32% by 2030 [2], and similar energy policies are being implemented in many countries. Because most RESs are inverter-based resources (IBRs) and not having rotating masses, the system inertia has been decreased consistently. Coupled with the variability of RESs, the low inertia has become a serious problem for system-frequency stability [3,4].

The battery-type energy storage system (ESS) is considered as one of the solutions to cope with the fluctuations caused by RESs. To complement the remaining synchronous generators (SGs) in the system, research on frequency support through the ESSs has been actively conducted. Droop control, which is the inherited control strategy of governors, has been applied to ESSs [5]. However, this technique cannot make a meaningful contribution to the inertia of the system, and further adjustments are required after the frequency reaches a steady state. To increase the system inertia, many researchers have studied control strategies in which ESSs emulate the dynamics of conventional generating units;

this is normally called a virtual synchronous machine (VSM) [6–14]. When ESS outputs the power that is proportional to the rate of change of the frequency (ROCOF), it can operate as a VSM. Recently, the risk of excessive ROCOF is recognized, and the related grid code is being reorganized [15]. VSM strategies have the advantage of being able to improve the system ROCOF response. However, there are still drawbacks: an additional filter is needed for accurate measurement of the ROCOF [16], and each ESS operates individually without cooperation between facilities. Recently, there have been studies for ESSs cooperation control strategies. To optimize the state of the charge (SoC), ESSs have been aggregated, and communication between ESSs has been utilized [17,18]. However, all the frequency-support strategies of previous researches are based on response-driven frequency control (RDFC) [5–14,17,18]. Since facilities with RDFC operate according to frequency changes without judging what kind of accident has occurred, RDFC has a limitation compared with event-driven frequency control (EDFC), in which facilities immediately perform a frequency-support operation which is customized for the occurred event.

Event-driven control involves performing a predetermined operation on a target event. Statistical process control, which is based on previous data, is the representative type of event-driven control. Since ESSs with flexible power control are suitable for RDFC, EDFC is generally not used by ESSs. However, EDFC has been studied in the field of under-frequency load shedding (UFLS) [19–21]. A method was proposed for predicting the magnitude of disturbance with the ROCOF according to the generator outage data and performing load shedding depending on the disturbance [19]. In another study, an extreme learning machine trained with operating conditions and contingencies has been used to derive the necessary load shedding when an actual contingency occurred [20]. There has been a load-shedding scheme that is based on an active and reactive power change [21]. In [20,21], a machine-learning algorithm was used to predict proper load shedding.

The main difference between ESS frequency control and UFLS is the possibility of continuous control. Load recovery after the load shedding has normally not been considered in studies on UFLS. However, because the ESSs are relatively free of power output variations, returning the output to its original operating point can be considered; i.e., not only the magnitude but also the duration of the ESSs output can be considered as a variable. If the frequency can remain stable even when the ESS stops the control action after a certain duration, there is no need for ESSs to maintain the output. In contrast, if the frequency becomes unstable when ESSs stop the control action, the output of ESSs should be maintained. The judgment of this requires information on disturbances and an understanding of the system frequency characteristics.

Although the frequency-response characteristics of the power system are highly nonlinear, they can be learned by a neural network. It can determine whether the ESSs should maintain the output or not according to frequency measurements in a short time. Additionally, the magnitude and duration of the ESSs output for the desired frequency response can be estimated. Typically, the most important factor of the “desired frequency response” is the frequency nadir. That is, proposed EDFC enables ESSs to output the power that is just necessary for the desired frequency nadir under a specific disturbance. The main contribution of the proposed EDFC method is summarized as follows:

- (1) Event-driven strategy is applied for ESS control.
- (2) Whether ESSs should perform a control action to comply with the grid code under a specific disturbance can be judged.
- (3) With relatively low peak-power rated ESSs, the frequency grid code can be complied.
- (4) With reduced ESS energy consumption, the frequency grid code can be complied.

The remainder of this paper is organized as follows. In Section 2, the concepts of RDFC and EDFC are explained in detail and compared. In Section 3, the frequency dynamics are analyzed via a model-based approach to elucidate the frequency response in a case where the ESS power output suddenly stops. In Section 4, the organization of the neural networks and the overall control strategy are described. Additionally, the data-selection technique for good performance of the neural networks

and the consideration for generator outage situations are involved. In Section 5, the proposed control method is validated with the neural-network estimation performance test and simulation results.

2. EDFC with ESS

2.1. ESS Frequency Support

In response to the penetration of the RESs, the installation of ESSs has been increasing. There are various ESSs with different energy-storage methods, and most types are featured in flexible and fast power control. They are utilized to support the power system in a variety of ways. The general applications of ESSs are peak shaving, frequency regulation, microgrid, and renewable integration.

Among the applications, frequency-regulation ESSs are used to keep the system frequency within the stable region. Maintaining the system frequency is important, because excessive frequency deviation from the standard can adversely affect the power system equipment. For this reason, most countries have their own grid code associated with a frequency [22]. Since the inertia of power systems is presently decreasing as the conventional generators with inertia are replaced with IBRs, the importance of frequency-regulation ESSs is increasing.

2.2. RDFC vs. EDFC

In this study, ESS frequency control methods are divided into two: response-driven and event-driven. In the former, the ESS adjusts the output according to the measured frequency. ESSs and other power-electronic equipment with frequency control normally use response-driven method. The latter can be described as customized control. When a disturbance occurs, control is performed with the operating point precalculated or estimated. The scheme of the RDFC and proposed EDFC methods are shown in Figure 1. F_{meas} represents the measured frequency and P represent the output of the ESS. In RDFC, each ESS is individually controlled by a local frequency. In proposed EDFC, ESSs send equipment status information, such as SoC, to the central control system, which determines the operating point of each ESS according to the status and the event that occurred. This allows several ESSs to operate as one large ESS.

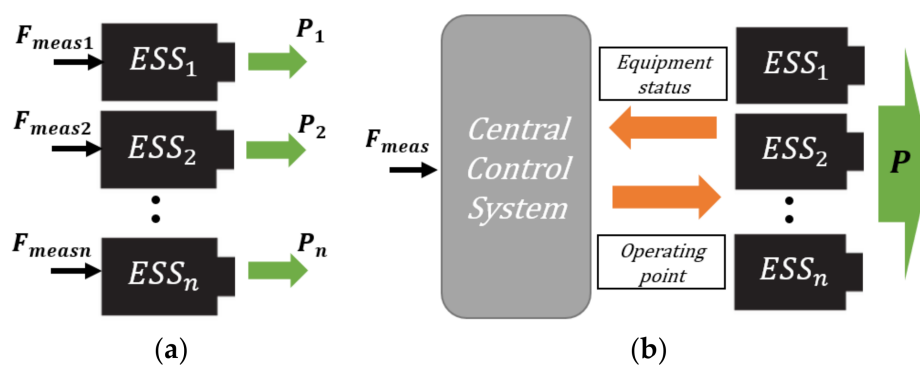


Figure 1. (a) Response-driven control; (b) Proposed event-driven control.

RDFC can be divided into droop control and synthetic inertia (SI) control, as shown in Figure 2. The parameters in Figure 2 are as follows: f represents the system frequency, f_{ref} represents the reference frequency of the control, T_m represents the time constant of the measurements, k_{dr} represents the droop-control gain, k_{si} represents the SI-control gain, P_0 represents the reference power without RDFC, and P_{ref} represents the practical reference power. The inputs of the droop control and SI control are the frequency error and ROCOF, respectively. In both controls, the output of the ESSs changes in proportion to the input. Here, the swing equation is reviewed for comprehension of the SI control dynamics. The difference between the mechanical power and electrical power of the SG is given by the

change in the kinetic energy of the SG rotor. The power absorbed by the rotor can be expressed in per unit magnitude as follows:

$$\Delta P_{rotor} = \Delta P_m - \Delta P_e = H \frac{df}{dt} \quad (1)$$

where ΔP_m represents the mechanical-power change, ΔP_e represents the electrical-power change, and H represents the inertia constant. When the ESS can change the power output in proportion to the ROCOF instantaneously, it can act as a synthetic rotor. Clearly, the SI-control gain k_{si} has the same dimension as the inertia constant H .

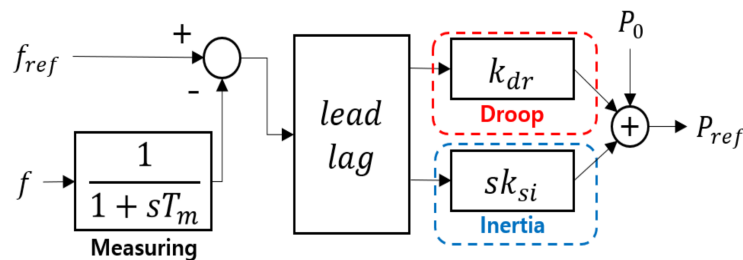


Figure 2. Block diagram of response-driven frequency control (RDFC).

Since RDFC uses the local measured frequency, it has the advantage that communication is not necessary; however, ESSs cannot cooperate with each other globally. Additionally, ESSs operate unnecessarily even under disturbances that do not violate the grid-code criteria, and the selection of the control parameters can be complex. EDFC based on credible data can alleviate these problems.

For EDFC to show the desired performance for a particular event, the following information is needed: the extent of the event and corresponding operating point of the ESSs to comply with the grid code. However, it is difficult to obtain the information accurately owing to the nonlinearity of the system frequency characteristics. In this case, a data-based neural network can be an appropriate solution. Only with short-time frequency data, the neural networks can estimate the information needed for EDFC. If the estimation is appropriate, the ESSs of the system can respond to the event immediately and optimally. The estimation method using neural networks is discussed in detail in Section 4.

3. System Frequency Response (SFR) with EDFC

In this section, the frequency response is analyzed via a model-based approach. Although the prediction of disturbances is impractical with a model-based approach, this analysis provides insight into the frequency change resulting from a disturbance as the ESS performs the proposed EDFC. The frequency response is approximated by a linear SFR model [23], as shown in Figure 3a. In Figure 3, ΔP_{ESS} represents the ESS output, ΔP_D represents the disturbance power, t_{du} represents the duration of the ESS control action, R represents the droop constant of the governor, F_H represents the high-pressure turbine ratio, and T_R represents the generator output time constant. All the variables are in per unit values. The MVA base is equal to the total rating of all the generating units in the system. In this study, the damping factor is ignored, and the disturbance power ΔP_D is always positive. It is assumed that the disturbance and the ESS control action occur simultaneously, because the EDFC process takes a relatively short time compared to the frequency dynamics. Additionally, it is assumed ESS stops the control action after a certain period of time (t_{du}).

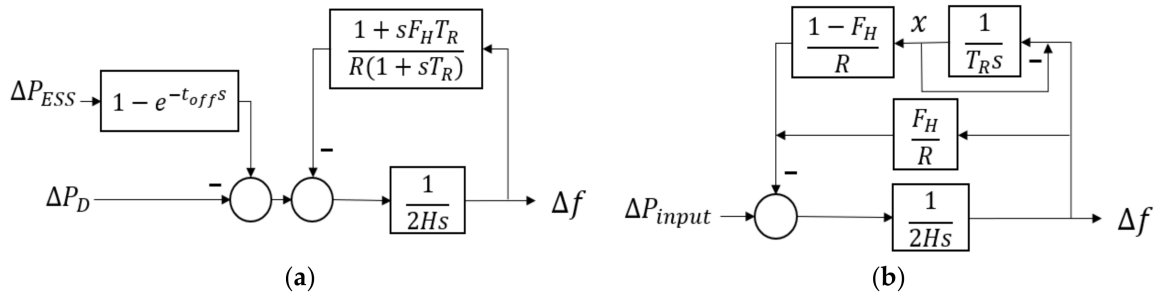


Figure 3. (a) Linear system frequency response (SFR) model. (b) Different form of the SFR model.

To make the state variable of the SFR model clearer, Figure 3a is modified as Figure 3b. When the state variables are frequency change (Δf) and x in Figure 3b, the differential equation of the SFR is as follows:

$$\dot{\Delta f} = \frac{1}{2H} \left(-\frac{F_H}{R} \Delta f - \frac{1 - F_H}{R} x + \Delta P_{input} \right) \tag{2}$$

$$\dot{x} = \frac{1}{T_R} (\Delta f - x) \tag{3}$$

Since the input (ΔP_{input}) before and after the ESS stops the control action is different, the time needs to be divided into two intervals for time-domain analysis. The inputs in the first and second intervals are $\Delta P_{ESS} - \Delta P_D$ and $-\Delta P_D$, respectively. Since the initial values of the state variables are zero in the first interval but not in the second interval, they must be considered when solving the differential equation in the second interval. The development of differential equations is described in Appendix A, and the result is as follows:

$$\Delta f(t) = \begin{cases} R(-\Delta P_D + \Delta P_{ESS}) \left(1 + a e^{-\xi \omega_n t} \sin(\omega_r t + \theta_1) \right) & t < t_{du} \\ \Delta f_{t_{du}} + (-R\Delta P_D - \Delta f_{t_{du}}) \left(1 + \beta e^{-\xi \omega_n (t - t_{du})} \sin(\omega_r (t - t_{du}) + \theta_2) \right) & t \geq t_{du} \end{cases} \tag{4}$$

where ω_n represents the natural frequency; ξ represents the damping ratio; ω_r represents the damped frequency of oscillation; θ_1 and θ_2 represent the initial phase in the first and second intervals, respectively; $\Delta f_{t_{du}}$ represents the frequency change when the ESS stops the control action; and α and β are constants multiplied by the transient component in the first and second intervals. Detailed formulas for each parameter are presented in Appendix A.

The frequency change in each interval consists of a dc component and a transient component. The frequency nadirs exist in the respective intervals, and they are the sum of the dc component and the first minimum of the transient component in its interval. The components of the first nadir (FN) are presented in Figure 4a, where f_0 represents the initial value of the frequency and m_t represents the first minimum of the transient component described in Appendix A.

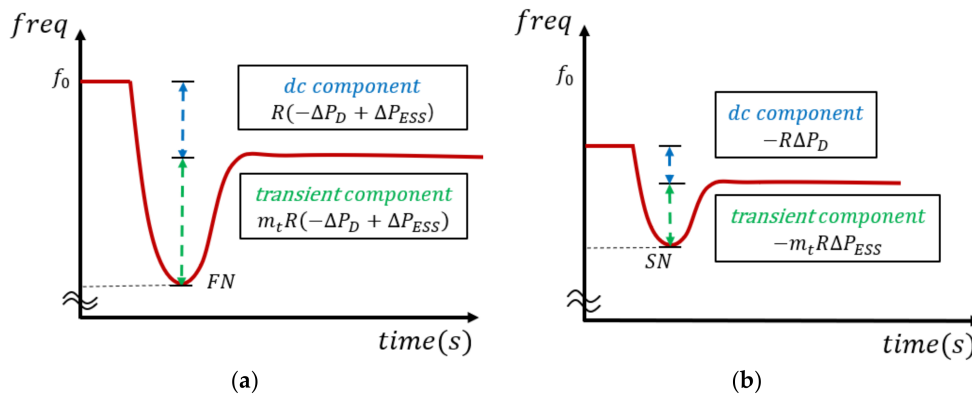


Figure 4. Components of the frequency nadir in the (a) first interval and (b) second interval.

The two variables that the system operator can handle are the magnitude and duration of the ESS output. According to Equation (4), the FN is dependent on the magnitude of ESS output. In the case of limitless ESS output, the FN can be easily adjusted as intended by the system operator. In contrast, the second nadir (SN), which is affected by both the magnitude and duration, is not easy to adjust. Because the parameters of the second interval change with respect to the initial value of the state variable, the SN is difficult to analyze. However, the fact that state variable x is equal to the frequency change in the steady-state significantly simplifies the second-interval parameter. In a steady state, the parameters of the second interval become equal to those of the first interval, and $f_{t_{du}}$ becomes $R(-\Delta P_D + \Delta P_{ESS})$. When x is equal to Δf at t_{du} , the components of the SN are presented in Figure 4b. Furthermore equation (4) can be simplified as follows:

$$\Delta f(t) = \begin{cases} R(-\Delta P_D + \Delta P_{ESS})(1 + ae^{-\xi\omega_n t} \sin(\omega_r t + \theta_1)) & t < t_{du} \\ -R\Delta P_D - R\Delta P_{ESS}ae^{-\xi\omega_n(t-t_{du})} \sin(\omega_r(t-t_{du}) + \theta_2) & t \geq t_{du} \end{cases} \quad (5)$$

Additionally, the FN and SN can be simplified as follows:

$$FN = f_0 + R(-\Delta P_D + \Delta P_{ESS})(1 + m_t) \quad (6)$$

$$SN = f_0 - R(\Delta P_D + m_t \Delta P_{ESS}) \quad (7)$$

The nadir without control ($\Delta P_{ESS} = 0$) is expressed as follows:

$$f_{ncnd} = f_0 - R\Delta P_D(1 + m_t) \quad (8)$$

Unless the ESS output exceeds the disturbance, both the FN and the SN are larger than the nadir without any frequency support control. However, as the ESS output increases, although the FN increases, the SN decreases. Since the actual nadir is the smaller of the two values, the optimal nadir is obtained when the FN and the SN are equal. Here, the optimal nadir means the best nadir on the condition that the ESS stops the control action in the middle. When Equations (6) and (7) are identical, the magnitude of the ESS output at the optimal nadir can be obtained as follows:

$$\Delta P_{ESS} = \frac{\Delta P_D}{1 + 2m_t} \quad (9)$$

Substituting Equation (9) into Equation (7) yields the optimal nadir:

$$f_{opnd} = f_0 - \frac{1 + 3m_t}{1 + 2m_t} R\Delta P_D \quad (10)$$

When the ESS output decreases with a sufficient time constant (not a step response), the frequency response can improve. However, the rate of change of the output should be excessively slow, similar to the case of maintaining the output. When the optimal nadir for a particular disturbance is lower than the grid-code criteria, the ESS should maintain the output until the automatic generation control (AGC) intervenes.

4. ESS EDFC Using Neural-Network Estimation

In this section, an EDFC strategy using neural networks is introduced. The objectives of the neural networks are not only to predict the extent of the disturbance but to determine the corresponding magnitude and duration of the ESS output. The first subsection introduces the neural-network structure and overall control scheme. The second subsection introduces the data-selection method. The third subsection deals with the generator-tripped case.

4.1. Neural Network Structure and Control Scheme

As illustrated in Figure 5, two neural networks are used: NN1 and NN2. NN1 has one input and three outputs, and NN2 has three inputs and two outputs. The description of the new parameters related to NNs are as follows: t_f represents the time at which the frequency reaches two threshold frequencies, f_{nd} represents the frequency nadir without control, f_{ss} represents the steady-state frequency without control, and FNR and SNR represent the references of the FN and SN.

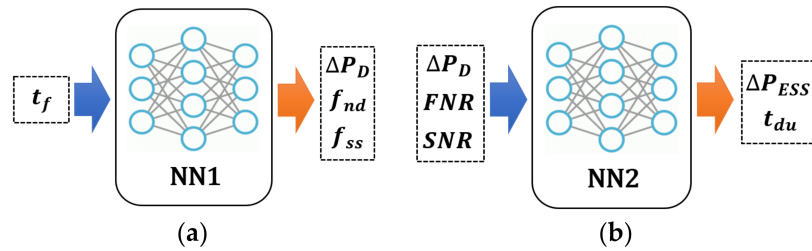


Figure 5. Neural-network structure for the proposed control (a) NN1, (b) NN2.

I/O values are visualized in Figure 6. NN1 estimates the ΔP_D , f_{nd} , and f_{ss} from t_f . According to Equation (1), the system power difference is proportional to the ROCOF; thus, the ROCOF can be an ideal variable for predicting the extent of the disturbance. However, because the instantaneous ROCOF can be considerably affected by noise during the measurement process, the average ROCOF can substitute it. There are two threshold frequencies in Figure 6: f_{th1} and f_{th2} . The average ROCOF can be determined as follows:

$$ROCOF_{avg} = \frac{f_{th2} - f_{th1}}{t_f} \tag{11}$$

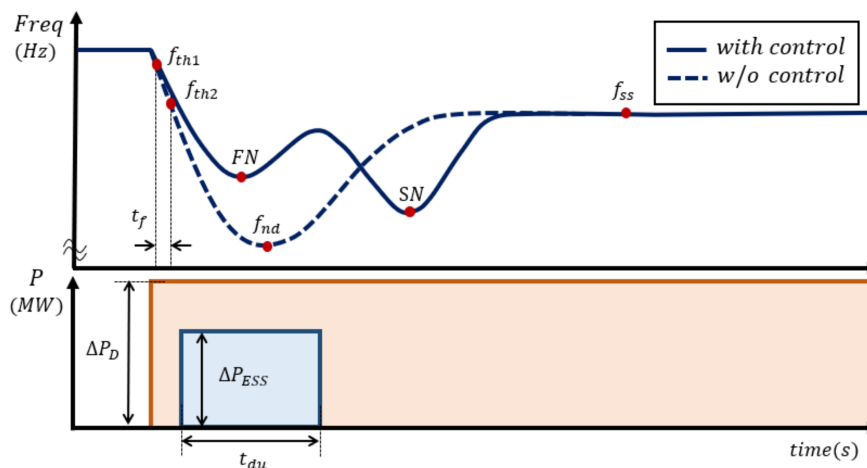


Figure 6. Frequency response with the I/O values.

When the t_f is sufficiently small, the difference between the average ROCOF and the instantaneous ROCOF can be ignored. That is, t_f involves sufficient information to predict the three outputs.

Each estimated value of NN1 is used as a control signal. ΔP_D is used as the input for the NN2. When predicted f_{nd} does not violate the grid-code criteria, the ESS does not need to perform any control. In this method, unnecessary operation of the ESS can be prevented. The f_{ss} can determine whether to maintain the output of the ESS until the AGC operates. According to Equation (4), the steady-state frequency due to a disturbance can be expressed as:

$$f_{ss} = f_0 - R\Delta P_D \tag{12}$$

The optimal nadir can be obtained by substituting Equation (12) into Equation (10). When the optimal nadir is lower than the grid-code criteria, the ESS should continue the control action until there is an adjustment by the AGC. Nonetheless, the system frequency would violate the grid code.

NN2 estimates the magnitude (ΔP_{ESS}) and duration (t_{du}) of the ESS output corresponding to the occurred disturbance (ΔP_D) to form the intended nadir (FNR, SNR). The inputs are the predicted ΔP_D , FNR, and SNR. Both nadir references must be higher than the grid-code criteria. Since ΔP_{ESS} and the FN are highly correlated, corresponding ΔP_{ESS} can be relatively accurately estimated. However, estimation of t_{du} is more complex due to the relatively low correlation with SN. Therefore, proper data selection is more important for estimation of the duration than for estimation of the magnitude.

The overall control scheme is shown in Figure 7. The time count (t_{count}) starts after the frequency reaches the first threshold frequency (f_{th1}). When the frequency does not reach the second threshold (f_{th2}) for a long time, it can be judged that the disturbance is not large enough. In this case, the reference frequency (f_{ref}) is updated to the currently measured frequency (f_m), and the time count is reinitialized to zero. In the case where the frequency reaches the second threshold, t_f is obtained, and the neural-network estimation is performed with it. In neural network operation, the control signal determination process is shown in Figure 8a. When the frequency reaches a steady state after the disturbance occurs, it is necessary to update the frequency reference, and the time count is reinitialized.

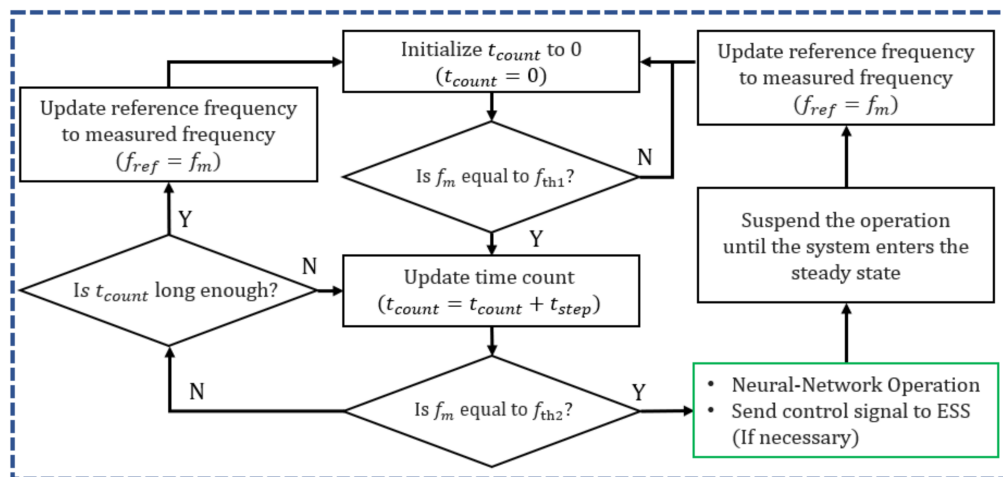


Figure 7. Control scheme of the central control system.

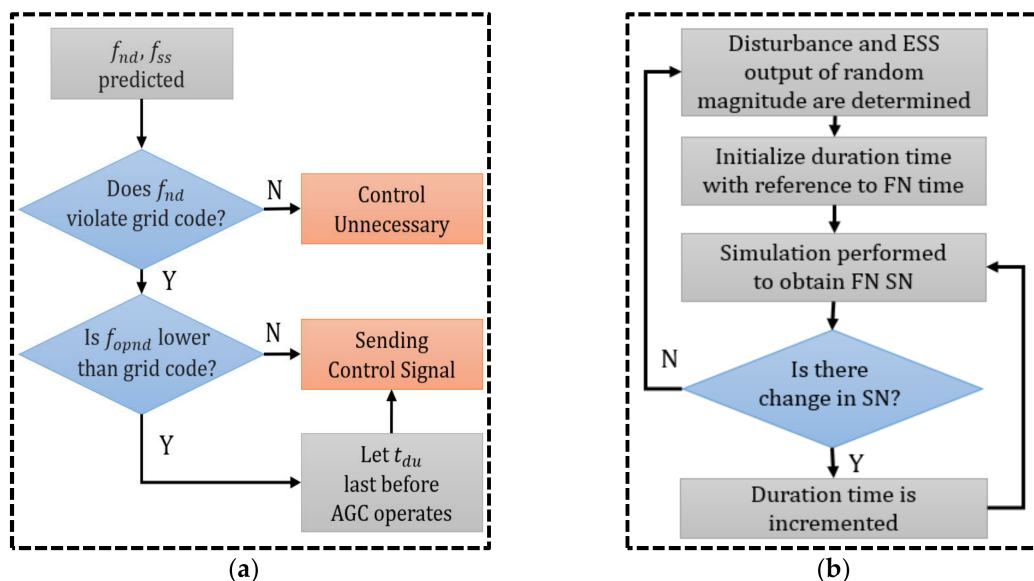


Figure 8. (a) Control signal determination process and (b) data selection algorithm for training NN2.

4.2. Data Selection for Accurate Estimation

The most important factor for the good performance of neural networks is the training data quality. For data to be high-quality, the output variation caused by the input variation must be noticeable. The correlation between the ROCOF and the disturbance power is obvious. Similarly, there are clear relationships between other inputs and outputs except the SN and t_{du} . When the frequency reaches a steady state during the ESS control, there is no change in the SN, irrespective of the extent to which the t_{du} increases. If the dataset contains many examples where the frequency reaches a steady state before the ESS stops the control action, the neural network encounters difficulty in estimating the duration of the ESS power for the reference SN. To prevent it, the data must be filtered. The data filtering algorithm is presented in Figure 8b.

The process of obtaining the data is as follows. First, the disturbance and ESS output of a random magnitude are determined. There is a constraint that the magnitude of the ESS output is lower than the magnitude of the disturbance. Then, the simulation is performed for the target system iteratively as the duration of the ESS output is incremented. When the SN does not change anymore, it can be judged that the steady state has been reached, and subsequent simulation examples are invalid data. Then, the simulation environment is changed to a new disturbance and ESS output. By this algorithm, a high-quality dataset for accurately predicting the duration can be built.

4.3. SG Tripped Condition

In the case of disturbance accompanied by a generator outage, additional information is needed for a desired performance of the proposed EDFC. Since the estimation of the neural networks is highly dependent on the SG status in the system, the central control system needs to instantly acquire the information about the operating status of the generating units.

The neural-network estimation is based on the frequency characteristics of a particular system. Disturbances such as a momentary fluctuation of the RES power does not affect the estimation of the neural networks, even though the magnitude is significantly large. However, when the inertia and droop dynamics change, the intended frequency response may not be obtained with the original neural networks trained with normal-state data. Therefore, the neural network should be trained for all possible generator outages, and a neural network tailored for a current system status should be utilized.

5. Simulation Result

The dataset-building process and the case studies was performed for the IEEE 39 bus system by using the Power System Simulator for Engineers. The ESS was modeled as a lumped element with no capacity limitations, and the bandwidth of the active power control was set as 1.6 Hz. f_{th1} and f_{th2} were set to 59.95 Hz and 59.9 Hz. The generator and governor models were the same for all ten generators in the system: GENTPJU1 and IEESGO, respectively. Additionally, for all the generators, the inertia constant and droop constant were 3.0 and 0.05, respectively. Information about the generator rating and operating point is presented in Table 1.

Table 1. Generator ratings and power outputs.

| | G#30 | G#31 | G#32 | G#33 | G#34 | G#35 | G#36 | G#37 | G#38 | G#39 |
|-------------------|------|-------|------|------|------|------|------|------|------|-------|
| S_{rated} (MVA) | 275 | 836 | 843 | 1175 | 1080 | 1085 | 1025 | 970 | 1684 | 1200 |
| P_{output} (MW) | 224 | 572.9 | 650 | 632 | 508 | 650 | 560 | 540 | 830 | 750.5 |

It is necessary to analyze the time taken for the proposed control action to be applied in real-time. Measurement of the time for the frequency to reach f_{th2} is required to estimate the desired operation action of ESSs. When a disturbance that slightly violated the grid code occurred in the system, the time it took for the frequency to reach f_{th2} was about 150 ms. In addition, the time for the central control

system to receive the generator trip information and to send the control signals to the ESSs needed to be considered. In [24], the signal propagation time on a 200-km-long fibre optic cable was assumed to be 1 ms. Eventually, the time from the occurrence of the disturbance to the ESS control actions was assumed to be 300 ms with enough margin in the study.

For building the dataset for NN training, a simulation was performed. While ESS control was involved in the simulation for the NN2 dataset, it was not involved in the simulation for the NN1 dataset. When a random-magnitude disturbance occurs in the system without frequency support control, the frequency change is as the dashed line in Figure 6. P_D , t_f , f_{pnd} , and f_{pss} constitute one example of the dataset for NN1. In the simulation for the NN2 dataset, the disturbance, the magnitude, and the duration of the ESS output were decided randomly. There were constraints that the ESS power was smaller than the disturbance ($\Delta P_{ESS} \leq \Delta P_D$) and the ESS power maintained at least until the FN appears. The frequency change is as the solid line in the Figure 6. ΔP_D , ΔP_{ESS} , t_{du} , FN, and SN constitute one example of the dataset for NN2. The disturbances are divided into two types: only a load change and a load change with a generator trip. The neural network was trained for both types.

5.1. Neural Network Training Results

The neural network model used in the study was an open-source model provided by MATLAB. The Levenberg-Marquardt training algorithm was employed, and the training parameters are presented in Table 2. All other parameters were default values in MATLAB.

Table 2. Neural networks training parameters.

| Parameter | NN1 | NN2 |
|-----------------------|---------------------|---------------------|
| Algorithm | Levenberg-Marquardt | Levenberg-Marquardt |
| Hidden layer (#) | 5 | 20 |
| Neurons per layer (#) | 10 | 10 |
| Epoch | 100 | 500 |

Each neural network has two datasets: normal-state and generator-tripped. The tripped generator was G #34 in the study. Each dataset for NN1 is composed of 300 examples: 200 examples constitute the training group, and 100 examples constituted the test group. Each dataset for NN2 is composed of 1000 examples: 700 examples constitute the training group, and 300 examples constituted the test group. The error rate between the test results and the actual values was calculated using the following formula:

$$err\% = \left| \frac{v_{real} - v_{test}}{v_{real}} \right| \times 100(\%) \quad (13)$$

Since the error rates differ by the training attempt, the average value after 10 training attempts was determined as the final neural-network error rate for a particular dataset. The error rates for NN1 and NN2 are presented in Table 3; Table 4.

Table 3. Results of the training test for NN1.

| - | Normal State | | | G#34-Tripped | | |
|----------------|--------------|----------|----------|--------------|----------|----------|
| | ΔP_D | f_{nd} | f_{ss} | ΔP_D | f_{nd} | f_{ss} |
| Error rate (%) | 0.24 | 0.123 | 0.088 | 0.143 | 0.048 | 0.067 |

Table 4. Results of the training test for NN2.

| - | Normal State | | G#34-Tripped | |
|----------------|------------------|----------|------------------|----------|
| | ΔP_{ESS} | t_{du} | ΔP_{ESS} | t_{du} |
| Error rate (%) | 0.068 | 2.66 | 0.07 | 3.738 |

The error rate for the three outputs of NN1 and the magnitude of the ESS out of NN2 is less than 1%. The prediction is highly accurate, and it can be inferred that is a strong correlation between the inputs and the outputs. In contrast, the error rate for the duration of the ESS output is relatively high (2%~3%). However, this is also a sufficiently meaningful prediction result and can be used for control in consideration of the error rate.

Table 4 presents the results of the training where data were selected using the dataset filter algorithm described in Section 4.2. Table 5 is the result of the training dataset, generated with a long duration limit of the ESS output in a normal state. The duration limit was set to 12 s. As the duration limit increases, the ESS maintains the output for a sufficient time, and the system is likely to reach a steady state. Since the SN does not change with the longer duration after the frequency reaches a steady state, an invalid dataset is generated, and it leads to a significant error rate for the duration of the ESS power. It can be seen that the error rate for the neural network trained by poor-quality dataset is approximately 10 times the error rate for neural network trained by the filtered dataset. Nevertheless, the error rate of the magnitude of the ESS output does not change. The reason is that the magnitude of ESS output is only correlated to the FN, which is determined independently of the duration of ESS output.

Table 5. Results of the training test for the normal-state with the invalid dataset.

| - | Bad Data Case | |
|-----------------|---------------|----------|
| Output variable | P_{ESS} | t_{du} |
| Error rate (%) | 0.071 | 29.183 |

5.2. Energy Consumption of the ESS by FN and SN Reference

A key feature of the proposed control method is that the central control system can determine the desired frequency-nadir. A simulation was performed to find the appropriate FNR and SNR values in this subsection. The disturbance was fixed, and the FN and SN values were collected as the magnitude and duration of the ESS output changed. Then, the examples that share the same frequency nadir among the data were chosen and the ESS energy consumption examined with respect to the formation of the FN and SN. The magnitude of the disturbance was set as 400-MW and 600-MW load change. The results are shown in Figure 9.

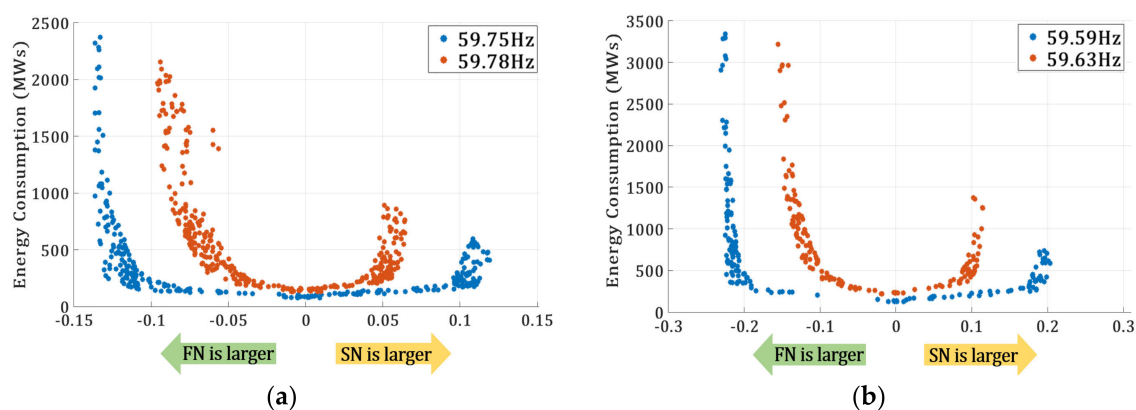


Figure 9. ESS energy consumption according to the FN and SN: (a) 400-MW load change and (b) 600-MW load change.

Here, one dot represents one example, and groups of same-color dots represents the examples that share the same nadir. The horizontal axis indicates the arrangement of the FN and SN. Zero indicates that the FN and SN have the same value. A positive value on the horizontal axis indicates that the SN is greater than the real nadir, and a negative value implies the opposite.

A high FN indicates that the magnitude of the ESS output is large and a high SN indicates that the magnitude is small and the duration is long. Because frequency nadir does not change when the duration is sufficiently long, there is a point at which only the energy consumption changes, not the FN and SN. In the graph, when the values of the FN and SN are close, the ESS energy consumption is modest. As indicated by the graph, the FNR and SNR should be set to the same value for achieving energy efficiency. Additionally, because the estimation of duration correlated to the SN has a relatively large error rate, it is necessary to set the SNR with a certain margin.

5.3. EDFC Performance with Different Nadir References

Here, the frequency-nadir criterion that the system must comply with is set to 59.5 Hz. The performance of the proposed control under a disturbance that violates the criterion is examined. However, the severe disturbance which forms the lower nadir than the optimal nadir of the proposed control is not considered. ESS EDFC was performed for three different nadir references: (59.5 Hz, 59.5 Hz); (59.6 Hz, 59.5 Hz); and (59.5 Hz, 59.6 Hz). A 700-MW load change occurred at 1 s, and the control action of the ESSs started at 1.3 s. The results are shown in Figure 10.

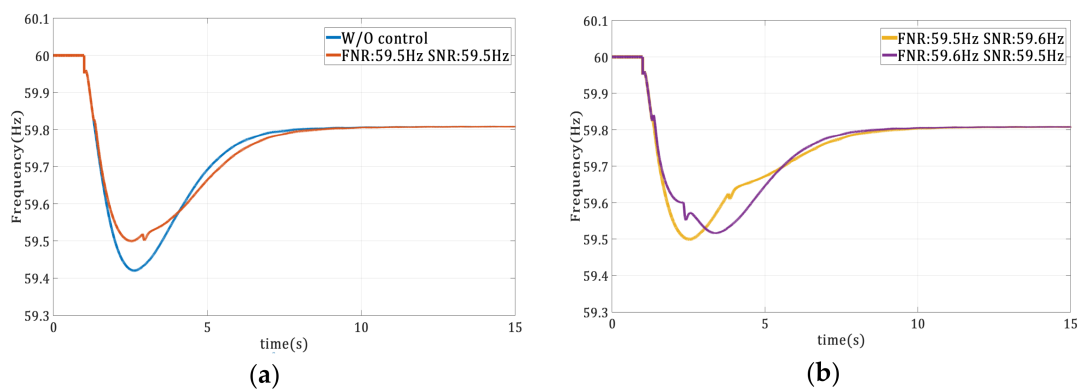


Figure 10. Frequency response for a 700-MW load change (a) without control, the EDFC with (59.5 Hz, 59.5 Hz); (b) EDFC with (59.6 Hz, 59.5 Hz); and EDFC with (59.5 Hz, 59.6 Hz).

The nadir decreases to approximately 59.4 Hz when the ESS do not support the frequency. When the EDFC is applied, the nadir is improved and formed near the reference value. In particular, the FN is nearly identical to the reference in all three cases where the EDFC is applied. However, for the SN, there is a small error, indicating a trend similar to that described in Section 5.1. The output of the ESS is presented in Figure 11. In consideration of the error rate of the duration of the ESS output, it is desirable to set the SNR to a higher value than the FNR with a margin.

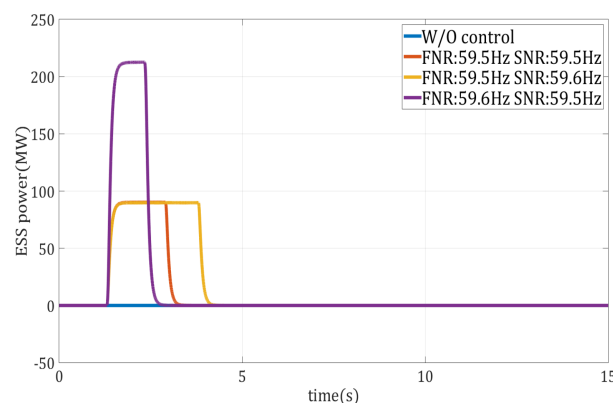


Figure 11. The power output of the ESS when performing the EDFC.

5.4. Comparison with Conventional Methods

Since the ESS EDFC is a noble strategy that has not existed before, the proposed method is compared with the conventional ESS RDFC methods: droop control and SI control. Each method is described in Section 2.1. For comparison of the three methods, the RDFC parameters were adjusted to form the same nadir for the same disturbance. The control gain and deadband range of the RDFC methods are presented in Table 6. As the previous case study, a load change of 700 MW occurred. Frequency and ESS output for three different methods are shown in Figure 12.

Table 6. Control parameters of conventional control methods. SI: synthetic inertia.

| Parameters | Droop Control | SI Control |
|--------------------|---------------|------------|
| Control gain k | 19 | 40 |
| Deadband (\pm) | 0.05 Hz | 0.03 Hz/s |

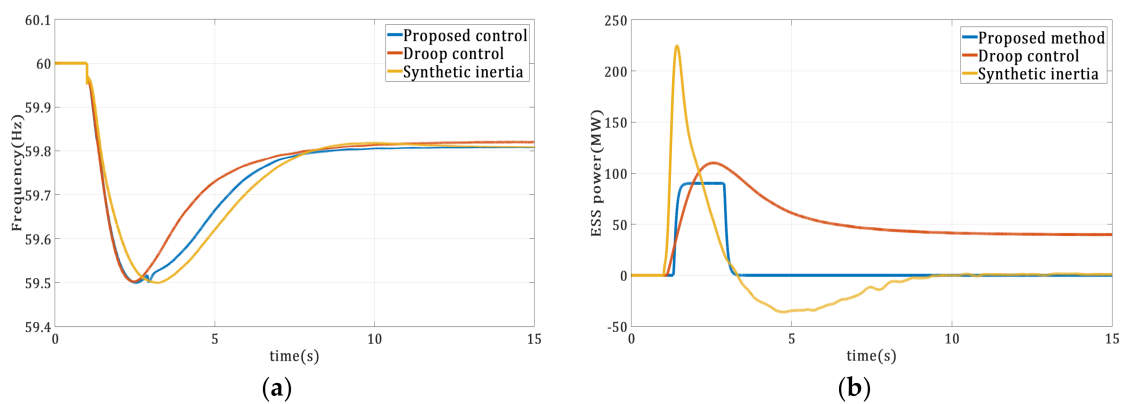


Figure 12. Comparison of three methods for a 700-MW load change (a) frequency and (b) ESS output.

All methods form the same frequency nadir for the same disturbance, but the corresponding ESS outputs are different. In droop control, it can be seen that the ESS maintains the output even in a steady state. In the SI control, the maximum output of the ESS is relatively high. In the proposed method, the energy consumption is reduced by stopping the control action in the middle, and the maximum output is also small.

When a modest disturbance which does not violate the grid code occurs, the results are shown in Figure 13. The disturbance was a 200-MW load change. The frequency nadir is formed near 59.9 Hz, which is not a severe value even when the ESS do not perform any control action in the proposed method. However, it can be seen that the ESS discharged power in the conventional methods. It can be concluded that the ESS is more efficiently controlled by the proposed method in the case study.

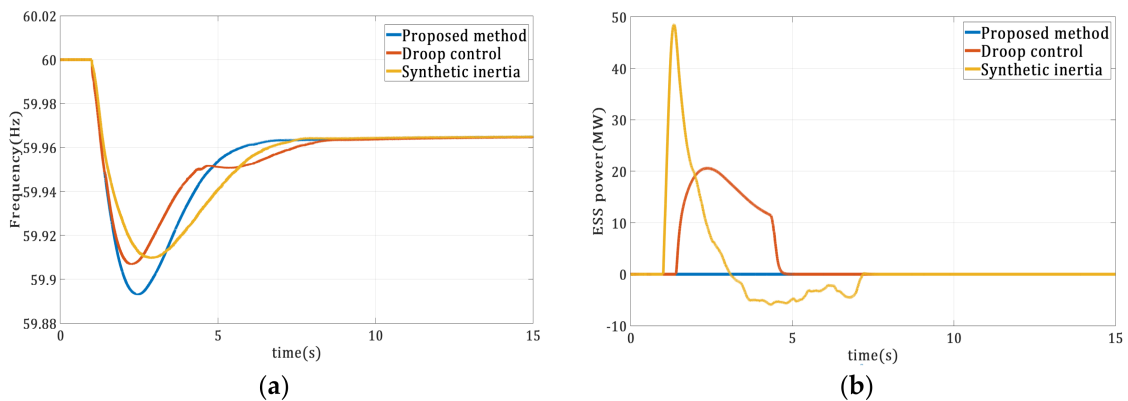


Figure 13. Comparison of three methods for a 200-MW load change (a) frequency and (b) ESS power.

5.5. Generator-Tripped Case

A simulation was performed for the case where the generator is tripped. The disturbance magnitude is 700 MW, the same with the simulation described in Section 5.3. However, the power of G#34 is included. The results for the normal-state neural networks and the customized neural networks for the contingency (G#34 trip) are compared. The nadir references of the normal NN and the customized NN are the same: (59.5 Hz, 59.5 Hz). The result is presented in Figure 14.

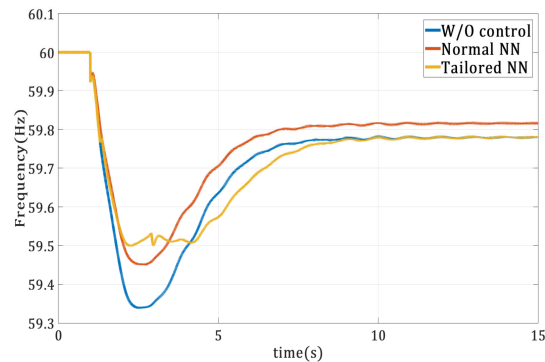


Figure 14. The frequencies for generator trip and load change (700 MW).

Although the magnitude of disturbance was the same with the previous case study (700 MW), the nadir is much lower when frequency support is not applied, owing to the SG trip, resulting in an inertia decrease. Additionally, the estimation of neural networks trained with the normal-state dataset is not accurate, and the frequencies violated the frequency grid code (59.5 Hz). In contrast, the estimation of the tailored neural networks trained with the dataset for the contingency is accurate. It indicates that the neural networks need to be trained for each possible contingency, and generator trip information is needed for a desired performance.

6. Conclusions

In this paper, a noble ESS EDFC strategy using neural networks was proposed and verified using the IEEE 39 bus system. The neural networks were trained with a dataset consisting of numerous examples according to the disturbance in the system. After the training, the neural networks predicted the severity of the occurred disturbance and estimated the customized operating action of the ESSs. The test results indicated the estimation accuracy of the neural networks was sufficient to be used for practical use. The validate simulation was performed in PSS/e using the control action of the ESS provided by the neural-network estimation. The results showed the frequency nadir with the EDFC was nearly identical to the reference nadir set by the operator—in other words, estimating the required action of the ESS for grid code compliance.

The proposed control prevents the ESSs from operating unnecessarily under a small disturbance which does not violate the grid code. Furthermore, if there is a more severe disturbance that violates the grid code, ESSs can use minimal energy to comply with the grid code by stopping the control action by the signal of the central control system in the proposed EDFC. This feature is a huge advantage compared to the RDFC. The proposed strategy is expected to be utilized in the optimal design and operation of frequency-regulation ESSs in a highly variable future system with large-scale RESs.

Author Contributions: Conceptualization and writing-original draft preparation, S.J.; data curation, J.L.; writing-review and editing, M.Y.; supervision, G.J. All authors have read and agreed to the published version of the manuscript.

Funding: This research received no external funding

Acknowledgments: This work was supported by the “Human Resources Program in Energy Technology” of the Korea Institute of Energy Technology Evaluation and Planning (KETEP) and granted financial resources from the Ministry of Trade, Industry & Energy, Republic of Korea (No.20194030202420).

Conflicts of Interest: The authors declare no conflict of interest

Appendix A

In the absence of an initial value, the Laplace transform of differential Equations (2) and (3) can be expressed as follows:

$$\Delta F(s) = \frac{R\Delta P_{input}(1 + T_{RS})}{s(2HRT_{RS}^2 + (2HR + F_H T_R)s + 1)} \quad (A1)$$

$$X(s) = \frac{1}{1 + T_{RS}} \Delta F(s) \quad (A2)$$

Equation (A2) indicates that the state variable x is a delay component for the frequency change. Equation (A1) can be expressed as follows using the standard form of the second-order delay element:

$$\Delta F(s) = \frac{R\Delta P_{input}(1 + T_{RS})}{s(s^2 + 2\xi\omega_n s + \omega_n^2)} \quad (A3)$$

If the power input (ΔP_{input}) is the sum of the ESS output and disturbance power ($\Delta P_{ESS} - \Delta P_D$), the inverse Laplace form of Equation (A3) becomes Equation (4) when $t \leq t_{du}$. The parameter of Equation (4) when $t \leq t_{du}$ can be expressed as follows by using the governor and generator parameters:

$$\begin{aligned} \omega_n &= \frac{1}{2HRT_R} & \xi &= HRT_R F_H \omega_n & \omega_r &= \omega_n \sqrt{1 - \xi^2} \\ \alpha &= \sqrt{\frac{1 - 2T_R \xi \omega_n + T_R^2 \omega_n^2}{1 - \xi^2}} & \theta_1 &= \tan^{-1}\left(\frac{-\sqrt{1 - \xi^2}}{\omega_n T_R - \xi}\right) \end{aligned}$$

To determine the time at which the nadir occurs, the first minimum of the transient component must be obtained. The transient component of Equation (4) when $t \leq t_{du}$ is as follows:

$$\Delta f_{transient}(t) = \alpha e^{-\xi\omega_n t} \sin(\omega_r t + \theta_1) \quad (A4)$$

Differentiating Equation (A5) yields

$$\begin{aligned} \dot{\Delta f}_{transient}(t) &= -\alpha\omega_n e^{-\xi\omega_n t} \sin(\omega_r t + \theta_x) \\ \text{where } \theta_x &= \theta_1 + \tan^{-1}\left(\frac{-\sqrt{1 - \xi^2}}{\xi}\right) \end{aligned} \quad (A5)$$

The first time Equation (A6) becomes zero is the time at which nadir occurs. It is given as

$$t_{min} = -\frac{\theta_x}{\omega_r} \quad (A6)$$

Substituting Equation (A7) into Equation (A4) yields the first minimum point of the transient:

$$m_t = -\alpha e^{-\xi\omega_n t_{min}} \sqrt{1 - \xi^2} \quad (A7)$$

If the initial values exist in Equations (3) and (4), the inverse Laplace transform for the frequency change is obtained as follows:

$$\begin{aligned} \Delta F(s) &= \frac{\Delta f_{t_{du}}}{s} + \frac{(R\Delta P_{input} - \Delta f_{t_{du}})(1 + T_{RS})}{s(2HRT_{RS}^2 + (2HR + F_H T_R)s + 1)} \\ \text{where } T_{RS} &= \frac{R\Delta P_{input} T_R - F_H T_R \Delta f_{t_{du}} - (1 - F_H) T_R x_{t_{du}}}{R\Delta P_{input} - \Delta f_{t_{du}}} \end{aligned} \quad (A8)$$

where $x_{t_{du}}$ represents the initial value of state variable x . If the power input (ΔP_{input}) is the disturbance power ($-\Delta P_D$), the inverse Laplace form of Equation (A3) becomes Equation (4) when $t \geq t_{du}$. Here,

$\beta = \sqrt{\frac{1-2T_R\xi\omega_n+T_R^2\omega_n^2}{1-\xi^2}}$ and $\theta_2 = \tan^{-1}\left(\frac{-\sqrt{1-\xi^2}}{\omega_n T_{RS}-\xi}\right)$. When the ESS power output lasts for a sufficient time and $x_{t_{du}}$ is equal to $\Delta f_{t_{du}}$, T_{RS} becomes equal to T_R and, accordingly, α and β become the same.

References

1. Bloomberg News Editors China Sets New Renewables Target of 35 Percent by 2030. Available online: <https://www.renewableenergyworld.com/2018/09/26/china-sets-new-renewables-target-of-35-percent-by-2030/#gref> (accessed on 26 September 2018).
2. Vaughan, A. EU Raises Renewable Energy Targets to 32% by 2030. Available online: <https://www.theguardian.com/business/2018/jun/14/eu-raises-renewable-energy-targets-to-32-by-2030> (accessed on 14 June 2018).
3. Ingleson, J.W.; Ellis, D.M. Tracking the eastern interconnection frequency governing characteristic. In Proceedings of the IEEE Power Engineering Society General Meeting, San Francisco, CA, USA, 16 June 2005; pp. 1461–1466.
4. IEEE P 1159 Working Group. *Recommended Practice for Monitoring Electric Power Quality*; Technical report, Draft 5; 1994; Available online: http://ewh.ieee.org/conf/tdc/IEEE_1159_Update_Collins_T&D_2008.pdf (accessed on 2 April 2020).
5. De Brabandere, K.; Bolsens, B.; Van den Keybus, J.; Woyte, A.; Driesen, J.; Belmans, R. A voltage and frequency droop control method for parallel inverters. *IEEE Trans. Power Electron.* **2007**, *22*, 1107–1115. [CrossRef]
6. Kehler, J.H. Considerations for load as a virtual generator for grid security. In Proceedings of the 2003 IEEE Power Engineering Society General Meeting (IEEE Cat. No. 03CH37491), Toronto, ON, Canada, 13–17 July 2003; Volume 4, pp. 2289–2292.
7. Driesen, J.; Visscher, K. Virtual synchronous generators. In Proceedings of the 2008 IEEE Power and Energy Society General Meeting—Conversion and Delivery of Electrical Energy in the 21st Century, Pittsburgh, PA, USA, 20–24 July 2008; pp. 1–3.
8. Beck, H.P.; Hesse, R. Virtual synchronous machine. In Proceedings of the 2007 9th International Conference on Electrical Power Quality and Utilisation, Barcelona, Spain, 9–11 October 2007; pp. 1–6.
9. Visscher, K.; De Haan, S.W.H. Virtual synchronous machines (VSG's) for frequency stabilisation in future grids with a significant share of decentralized generation. In Proceedings of the CIRED Seminar 2008: SmartGrids for Distribution, Frankfurt, Germany, 23–24 June 2008; pp. 1–4.
10. Zhong, Q.C.; Weiss, G. Static synchronous generators for distributed generation and renewable energy. In Proceedings of the 2009 IEEE/PES Power Systems Conference and Exposition, Seattle, WA, USA, 15–18 March 2009; pp. 1–6.
11. Van Wesenbeeck, M.P.N.; De Haan, S.W.H.; Varela, P.; Visscher, K. Grid tied converter with virtual kinetic storage. In Proceedings of the 2009 IEEE Bucharest PowerTech, Bucharest, Romania, 28 June–2 July 2009; pp. 1–7.
12. Zhong, Q.C.; Weiss, G. Synchronverters: Inverters that mimic synchronous generators. *IEEE Trans. Ind. Electron.* **2010**, *58*, 1259–1267. [CrossRef]
13. Bevrani, H.; Ise, T.; Miura, Y. Virtual synchronous generators: A survey and new perspectives. *Int. J. Electr. Power Energy Syst.* **2014**, *54*, 244–254. [CrossRef]
14. Torres, L.M.A.; Lopes, L.A.; Moran, T.L.A.; Espinoza, C.J.R. Self-tuning virtual synchronous machine: A control strategy for energy storage systems to support dynamic frequency control. *IEEE Trans. Energy Convers.* **2014**, *29*, 833–840. [CrossRef]
15. Meng, L.; Zafar, J.; Khadem, S.K.; Collinson, A.; Murchie, K.C.; Coffele, F.; Burt, G. Fast Frequency Response from Energy Storage Systems—A Review of Grid Standards, Projects and Technical Issues. *IEEE Trans. Smart Grid* **2019**, *11*, 1566–1581. [CrossRef]
16. Kirkham, H.; Pandey, S. Is ROCOF measurable? In Proceedings of the 2018 IEEE Power & Energy Society Innovative Smart Grid Technologies Conference (ISGT), Washington, DC, USA, 19–22 February 2018; pp. 1–5.
17. Shim, J.W.; Verbič, G.; Kim, H.; Hur, K. On Droop Control of Energy-Constrained Battery Energy Storage Systems for Grid Frequency Regulation. *IEEE Access* **2019**, *7*, 166353–166364. [CrossRef]

18. Wang, Y.; Xu, Y.; Tang, Y.; Liao, K.; Syed, M.H.; Guillo-Sansano, E.; Burt, G.M. Aggregated energy storage for power system frequency control: A finite-time consensus approach. *IEEE Trans. Smart Grid* **2018**, *10*, 3675–3686. [[CrossRef](#)]
19. Banijamali, S.S.; Amraee, T. Semi-Adaptive Setting of Under Frequency Load Shedding Relays Considering Credible Generation Outage Scenarios. *IEEE Trans. Power Deliv.* **2018**, *34*, 1098–1108. [[CrossRef](#)]
20. Dai, Y.; Xu, Y.; Dong, Z.Y.; Wong, K.P.; Zhuang, L. Real-time prediction of event-driven load shedding for frequency stability enhancement of power systems. *IET Gener. Transm. Distrib.* **2012**, *6*, 914–921. [[CrossRef](#)]
21. Singh, A.K.; Fozdar, M. Event-driven frequency and voltage stability predictive assessment and unified load shedding. *IET Gener. Transm. Distrib.* **2019**, *13*, 4410–4420. [[CrossRef](#)]
22. Luo, X.; Wang, J.; Wojcik, J.D.; Wang, J.; Li, D.; Draganescu, M.; Miao, S. Review of voltage and frequency grid code specifications for electrical energy storage applications. *Energies* **2018**, *11*, 1070. [[CrossRef](#)]
23. Anderson, P.M.; Mirheydar, M. A low-order system frequency response model. *IEEE Trans. Power Syst.* **1990**, *5*, 720–729. [[CrossRef](#)]
24. Descloux, J.; Rault, P.; Nguéfeu, S.; Curis, J.B.; Guillaud, X.; Colas, F.; Raison, B. HVDC meshed grid: Control and protection of a multi-terminal HVDC system. In Proceedings of the CIGRÉ Session Paris (Paper B4-308), Paris, France, 26–31 August 2012; p. 10. Available online: https://e-cigre.org/publication/B4-308_2012-hvdc-meshed-grid-control-and-protection-of-a-multi-terminal-hvdc-system (accessed on 16 December 2019).



© 2020 by the authors. Licensee MDPI, Basel, Switzerland. This article is an open access article distributed under the terms and conditions of the Creative Commons Attribution (CC BY) license (<http://creativecommons.org/licenses/by/4.0/>).